

## Multispectral Observations of the Jovian Aurora

### Introduction

The upper atmospheres of the Earth and the outer planets form a screen on which precipitating charged particles, like the electron beam in a television, trace fleeting, but revealing patterns of visible, ultraviolet, infrared, and x ray emissions that offer valuable clues to processes occurring within the planetary magnetospheres. At Earth, years of in situ measurements, as well as ground based observations, have yielded a picture (still fuzzy) where the interaction of the solar wind with the magnetosphere of the Earth provides a complex path for the storage and release of energy during magnetic substorms; the ultimate manifestation of terrestrial auroral processes. More recent global imaging of substorm events from high above the Earth ( $> 3.5 R_E$ ) by Dynamics Explorer have made a unique contribution towards understanding the global and temporal evolution of such auroral events by providing a morphological perspective and by providing the crucial observational link that allows the separation of spatial and temporal variations inherent in the interpretation of in situ data. A similar role was played by the Hubble Space Telescope (HST) during the recent encounter of Ulysses with Jupiter February, 1992 in helping to define a new paradigm in Jovian auroral physics. The old paradigm portrayed Jupiter's magnetosphere as totally dominated by internal processes (ie. Io related tori, heavy ions, etc.) where energetic heavy ion precipitation in the inner magnetosphere was solely responsible for the observed auroral phenomena. Ulysses and HST portray a more Earth-like paradigm where electron acceleration in the outer magnetosphere near the boundary with the solar wind plays a distinct role in the formation of auroral hot spots, yet energetic heavy ions also enter into the picture [this paper; Dols et al., 1992] (similar to the role of the energetic ions from the terrestrial ring current during magnetic substorms). These heavy ions as a result of excitation during their transit through the atmosphere produce the x ray emissions observed in Roentgensatellit (ROSAT) x ray energy spectra.

The ultraviolet spectrometers on the Voyager 1 and 2 spacecraft [Sandel et al., 1979; Broadfoot et al., 1981] and the International Ultraviolet Explorer (IUE) spacecraft [Clarke et al., 1980; Yung et al., 1982] observed intense  $H_2$  Lyman and Werner band emissions from the Jovian atmosphere at high latitudes, thus providing evidence for auroral particle precipitation at Jupiter. Observations in the infrared [Caldwell et al., 1980; 1983] showed spatial dependencies similar to those at ultraviolet wavelengths. X ray emissions were seen by the High Energy Astronomical Observatory 2 (Einstein) in the Jovian auroral zone [Metzger et al., 1983]. Taken together, these observations provide indications of an aurora more than 100 times more powerful ( $> 10^{13}$  Watts) than Earth's, which has a strong influence on the high-latitude structure, dynamics, and energetics of the upper atmosphere of Jupiter.

Earlier observations of the Jovian x ray aurora [Metzger et al., 1983] and in situ measurements of energetic oxygen and sulfur [Gehrels and Stone, 1983] indicated that energetic sulfur and oxygen were precipitating into the high-latitude Jovian atmosphere and were largely responsible for the observed ultraviolet auroral emissions. Building on the earlier work concerning electron aurora [Waite et al., 1983], Horanyi et al. [1988] developed a quantitative

model of the interaction of energetic oxygen ions and atoms with an  $H_2$ , H atmosphere. The model results indicated that sulfur and oxygen emissions in the ultraviolet at 1256 and 1304 angstroms should be detectable with the IUE UV telescope. Subsequent observations and analysis, however, showed no detectable emission at 1304 angstroms and an uncertain detection at 1256 angstroms [Waite et al., 1988]. This lead Waite and colleagues to conclude that the bulk of the observable UV auroral emissions are probably due to electrons and that the ions that do precipitate are quite energetic ( $>300$  KeV/nucleon) and are responsible for the x ray emissions, but do not make a significant contribution to the ultraviolet auroral emissions.

The conclusion of Waite et al. [1988] was not readily endorsed by the Jupiter magnetospheric community, which continued to embrace the dominant role of heavy ion precipitation as a source for the Jovian aurora. Until recently little new observational information was available to allow a re-examination of the energetic ion paradigm. However, the recent Ulysses encounter with Jupiter and the coordinated HST auroral imaging campaign reported in this paper present new evidence for an expanded role for electrons and association of the energetic electron source with the Jovian magnetopause boundary. In addition, ROSAT observations confirm the role of energetic heavy ions in x ray production, but suggest that the source is limited to energies greater than 300 KeV/ nucleon and as suggested by Waite et al. [1988] comprises only a fraction of the measured ultraviolet emission. Thus, a new paradigm of Earth-like auroral processes appears to be emerging from these exciting new results.

### **Hubble Space Telescope Faint Object Camera Images: Observations and Analysis**

Three separate HST investigations were scheduled and carried out with the FOC using three different filter sets. They were: 1) Caldwell et al. (F140W & F152M), 2) Paresce et al. (F120M & F140W), and 3) Stern et al. (F130M & F140W). The observations were obtained from February 6-9, 1992 in the four days surrounding the Ulysses spacecraft's closet approach to Jupiter. The images reported here are from the Stern, McGrath, Waite, Gladstone, and Trafton investigation using the FOC in a  $f/96$  512 by 512 pixel mode (F96N512) with filters F130M and F140W that have a peak spectral response near 1280 angstroms. The field-of-view was  $11 \times 11$  arcseconds and the exposure time for each of the eight images was 18 minutes. The center of the field-of-view was offset 20 arcseconds toward the appropriate Jupiter rotational pole during each observation with a pointing accuracy of approximately 1 arcsecond. For a point of reference Jupiter's polar radius during the time of these observations was approximately 20.54 arcseconds. A summary of the images obtained is shown in Table 1 where we have listed the time of observation, the  $S_{III}$  longitude of the central meridian at the midpoint of the observation, the pole observed, the intensity of noticeable features in the image, the emission area, and a rough estimate of the range of the emission power (taking into account the low signal to noise ratio of the data, the difficulty in determining the physical area of the emission, and the uncertainties due to atmospheric absorption).

The determination of the auroral emission power requires that a convolution of the FOC wavelength dependent quantum efficiency (QE) and filter response functions be convoluted with

the auroral H, H<sub>2</sub> spectrum. This was accomplished by modeling both the altitude dependent Lyman alpha and H<sub>2</sub> Lyman and Werner production rate profiles [Waite et al., 1983] assuming a low latitude hydrocarbon vertical distribution [Gladstone and Skinner, 1989] and a precipitating electron spectrum consistent with those observed by Ulysses in the outer magnetosphere [Lanzerotti et al., 1992] and extended down to energies of 20 KeV (below the detector threshold of 44.9 KeV) with the same power law slope in the distribution. The extension to lower electron energies was performed to match the H<sub>2</sub> band color ratio (a measure of the lower energy extent of the precipitating electron distribution for a specified methane vertical profile) generally observed in the Jovian auroral zone [Yung et al., 1980; Waite et al., 1988]. These production rate values were then used as input to a radiative transfer code [Gladstone and Skinner, 1988] (for output see Figure 1a) and then passed through an FOC QE/filter response to produce the synthetic spectrum seen in Figure 1b. As you can see the F130M F140W filter pair responds to both Lyman alpha and Werner band emission near 1280 angstroms, whereas the Paresce images are more sensitive to Lyman alpha and the Caldwell images to Lyman emission near 1580 angstroms. The latter wavelength region is less susceptible to methane absorption, thus it's specification in the upper wavelength range of the Yung et al. [1980] H<sub>2</sub> band color ratio:

$$CR = \text{Intensity}(1557\text{-}1619 \text{ angstroms}) / \text{Intensity}(1230\text{-}1300 \text{ ang.})$$

A comparison of the relative spectral responses of the three different filter combinations is shown in Table 2. In order to verify that this approach for determining the integrated auroral flux from the limited bandpass 130M 140W combination was not overly sensitive to the assumed methane vertical profile or to the assumed electron energy spectrum used in the modeling we repeated the QE/filter convolution with a measured IUE Jovian auroral spectrum and got the same result to within 20%. We then used the predicted FOC count rates and compared them to the measured rates along with constants that define the telescope's effective area to estimate the power influx levels required to produce the observed auroral emissions (shown in Table 1).

Two images of the north auroral zone (NAZ) and six images of the south auroral zone (SAZ) were obtained over the 4 day span. Five images (1 of the NAZ, 4 of the SAZ) showed emission (>1 sigma) above the image dark count. These five images are shown in Figures 2a and 2b. The image has been processed using a 10 pixel box car average and the color bar has been dynamically stretched to provide a common intensity representation from image to image while at the same time maximizing contrast in the low signal to noise level images. The average background count rate in the five processed images was 0.598 +/- 0.088 counts per pixel, whereas the count rate on the planet without auroral emission was 0.0654 +/- 0.094 counts per pixel. This suggest, as the images indicate, that there is no statistically visible planet limb to aid in interpreting the planetary coordinates. The limb and auroral zone overlays that are shown are determined by constructing a planetary coordinate grid and two sets of auroral zones: 1) L=6, associated with the Io plasma torus, and 2) L=infinity, associated with the last closed magnetospheric field line using the O<sub>4</sub> magnetic field model [Acuna and Ness, 1976] and an IDL program written by Dr. Tim Livengood to process IUE spectra from Jupiter. The finite spread to the auroral zones shown are simply due to the rotation of the planet during the 18 minute exposure. Peak count rates on the images lie between 0.88 and 1.67 counts per pixel which

corresponds to auroral intensities between 20 and 50 kiloRayleighs (kR), yet the low sensitivity of the dual filter FOC combination sets a detection threshold range between 10 and 20 kR. As such only the brighter auroral features are visible in the images and low emission intensities over large areas can mask large uncertainties in the auroral power (See Table 1; image features 101b, 101c, 302b, and 402b where an attempt has been made to estimate the emission uncertainty associated with diffuse emissions over large areas. The selected regions are shown in Figure 3 where a 10 by 10 block average representation of the image with a box overlay designating the selected areas are shown and Table 3 where the average count values and their associated uncertainties are listed.)

The NAZ image (image #101 in Table 1) shows a bright central feature near the Central Meridian Longitude (CML= 163-173 degrees  $S_{III}$  longitude) and therefore a reasonable estimate of the  $S_{III}$  longitude of the emission feature can be estimated and lies between 160 and 173 degrees. The bifurcated nature of the source can be explained by either spatial (5 degrees of longitude) or temporal (10 minutes, due to planetary rotation during the exposure) variability in the source. The bright source location (image #101a) is most consistent with a middle magnetospheric source (halfway between  $L=6$  and the last closed magnetospheric field line), but a pointing uncertainty of about 1 arcsecond (the size of the marker for celestial N and E) spans the range of auroral zones considered and makes the designation tentative at best. Some weaker emission (image #101b) poleward and westward of the central bright spot is just barely visible above the background as is the area (#101c) to the east of the bright central spot. These areas may represent a weaker "polar oval" emission that is more clearly seen at longer wavelengths in the images of Caldwell et al. (EOS,??). The other NAZ image (#102) suffers from a high noise level that negates meaningful analysis.

The first SAZ image is (image #201 from Table 1). In this image most of the emission appears to lie along the limb of the planet, thus making it difficult to estimate the longitudinal position and intensity of the emission. The CML of this image is 43 degrees  $S_{III}$ . Most of the emission appears to lie near a longitude of 180 degrees (#201a, westward edge of auroral zone), but another weaker (?) zone appears near 0 degrees (#201b, eastward edge of the auroral zone). However, image #202 taken 1 hr 27 mn later at a CML longitude of 95 degrees shows emission from the center of the imaged auroral zone (near 100 degrees) and suggests that significant changes in the auroral zone morphology occurred in the intervening time period. The extent of the limb emissions are most consistent with an auroral zone size which corresponds to the boundary of the last closed field lines (ie., maps to near the magnetopause boundary). The intensities listed in Table 1 for this image are uncertain due to the presence of limb brightening effects.

The image pair 301 302 provide information about the temporal variability of the auroral emissions. Image #301 (CML=5 degrees) shows no detectable emission above the background. Whereas, image #302 (CML=56 degrees) shows a bright emission feature between 20 and 30 degrees; a region that should have been clearly visible if present 1 hr 28 mn earlier in image #301. This suggest over a factor of three variation in the auroral intensity during the time period spanned by these two images. Image #302 is also particularly interesting from a Ulysses

encounter point of view, since at the time of the image the HISCALE experiment [Lanzerotti et al., 1992] had just been turned on after closet approach and was observing precipitating energy fluxes of electrons on the order of  $1 \text{ erg cm}^{-2} \text{ s}^{-1}$  ( $\sim 20 \text{ kR}$  of emission corresponding to light blue areas just above the background) at the dusk edge of the planet ( $S_{III} \sim 305$  degrees,  $L \sim 16$ ). Although the conjugate auroral point is just off the field of view of the image a duskward extension of the diffuse auroral emission seen surrounding the central bright spot in an auroral band at  $L > 16$  is of a consistent brightest and location to correspond to the measured electrons of HISCALE. Again as in image 201 the auroral zone is more consistent with a mapping to  $L > 15$ , yet here again pointing uncertainties must be carefully considered. Once again as in image #101 the complex structure of the central bright emission features can be explained by a combination of temporal and spatial structure of the auroral precipitation zones. As a matter of fact in image #302 some of the structure must be spatial because the large separation ( $> 1$  arcseconds) of hot spots cannot be explained by rotation of a time variable source alone.

Finally the image pair 401 402 again illustrate both the temporal and spatial variability of the source. No detectable emission above background is seen in image #401 (CML=350-360 degrees), but 1 hr 26 mn later an emission (image #402a) appears near 300 degrees CML; a longitude range that should have been visible in image #401. The magnetic latitude in 402 is again more consistent with auroral emission that maps to the magnetopause boundary than with emission that maps to the Io plasma torus.

### **HST FOC Images: Discussion**

A major consideration in placing these HST FOC images in the context of past Voyager UltraViolet Spectrometer (UVS) and International Ultraviolet Explorer (IUE) observations is the low signal to noise ratio of the images and the resulting sensitivity threshold between 10 and 20 kR of emission over large areas of the high latitude region which would not be visible above the background. Clearly these images are a high spatial resolution tracer of the variations in the auroral bright spots and not as good of an indicator of the more diffuse auroral emission or correspondingly of the total auroral power output. Integrated power numbers for the input power required to produce these bright emissions range from  $10^{10}$  to  $10^{12}$  Watts in both the SAZ and NAZ. However, if we assume that a 20 kR band from 65 to 85 degrees may exist below the detection limit of the FOC then up to  $4 \times 10^{13} \text{ W}$  of input power may be present, but unaccounted for by the present observations. This also would imply that less than 10% of the emission is found in the bright spots, whereas Herbert et al.'s [1987] analysis of the Voyager data suggest that between 20 and 30% of the emission is concentrated in the bright auroral emission regions. Furthermore, Herbert et al. [1987] give estimates of the emitted power (in their Table 2) which can be used to estimate the input power using the emissions efficiencies given by Waite et al. [1983]. Their results give values for the total auroral power input for Voyager 1 inbound of  $1.2 \times 10^{14} \text{ Watts}$  and for the outbound  $4 \times 10^{13} \text{ Watts}$  and an estimate for Voyager 2 of  $1.1 \times 10^{14} \text{ Watts}$ . Livengood [1991] has performed an extensive analysis of the IUE Jovian aurora data set. Using the information from Figure 5.9 of Livengood [1991] and the modeled emission efficiencies from Waite et al. [1983] we obtain an average auroral H,  $\text{H}_2$  emission power of  $4.4 \times 10^{12} \text{ Watts}$  (both poles) and an input power of  $2.4 \times 10^{13} \text{ W}$  with a one sigma variance of  $\sim 1$

$\times 10^{13}$  Watts and individual data points that show up to a factor of six variation in the emitted power over the span of less than one month. The limited data set of Livengood [1991] spans over 10 years with relatively greater sampling since 1988, but there are no indications of a long term trend in the auroral power output. Placing the measured and inferred auroral power output of the FOC images in the context of the UVS and IUE data suggest that: 1) the majority of the emitted auroral power is in diffuse and weak features below the sensitivity threshold of the FOC, 2) the auroral output power during the Ulysses encounter was in the range of it's observed average as determined by IUE ( $1$  to  $3 \times 10^{13}$  Watts), and 3) the aurora is randomly time variable on time scales as short as 10 minutes (given a temporal interpretation of the bifurcation of the bright spot in image #101), and certainly varies by over a factor of three in brightness on time scales of hours.

The UVS and IUE data sets also indicate a systematic variation of the intensity of the auroral emissions in both the NAZ and SAZ as a function of  $S_{III}$  longitude. Although these bright regions are identified in the FOC data set (image #101 for the NAZ, central bright spot at  $\sim 170$  degrees; image #302 for the SAZ, central bright spot at  $\sim 25$  degrees), the considerable spatial and temporal variation that occurs in time spans of less than two hours in the set of eight FOC images reported here suggest a much more complex pattern of variability (at least for the brightest auroral emissions) and further suggest that part of the systematic variance from IUE and UVS may be due to geometrical considerations of a large spectrometer slit viewing an increasing area of diffuse and distributed auroral emission at certain preferred  $S_{III}$  longitudes.

Information on the spectral variations of the Lyman alpha and Lyman and Werner band systems cannot be inferred from the single filter set used in the reported FOC images. As a result, information about the  $H_2$  band color ratio as a function of longitude reported by both IUE and UVS, which gives information on the input particle energy spectrum and/or the changes in the hydrocarbon atmosphere, cannot be compared at present. However, by mixing the different images from the three sets of observations it may be possible to draw some conclusions about systematic variations in the emission spectrum (see Table 3). The one caveat is the high degree of variability will make any spectral comparison from one image to the next hard to quantify.

The most exciting new piece of information comes from the high spatial resolution that can be obtained from HST. The small bright discrete sources seen in the data set put obvious constraints on the magnetospheric processes responsible for the precipitating particles. This patchy and discrete structure is also present in the observed high-latitude magnetospheric particle populations observed by the HISCALE particle detector on the Ulysses spacecraft [Lanzerotti et al., 1992]. Furthermore, the location of the discrete features in latitude (although individually accurate to one arcsecond due to pointing uncertainties) collectively are consistent with a precipitating particle origin in the middle (NAZ) or outer (SAZ) magnetosphere, which is again consistent with the measurement by HISCALE of precipitating electrons in the middle and outer magnetosphere. The limited data available, however, make a comparison to Voyager UVS derived auroral zone [Herbert et al., 1987] difficult to carry and further HST observations are needed to verify the present result. The inference to be drawn from this information is that the Jovian aurora is more Earth-like than previously thought and that acceleration of electrons carrying field-aligned currents in the middle and outer magnetosphere may be largely responsible for the

discrete auroral emission features seen by HST in the southern auroral zone.

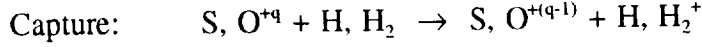
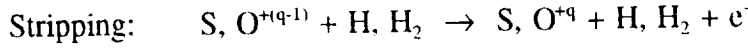
## ROSAT Observations

The ROSAT Position Sensitive Proportional Counter (PSPC) acquired nine data segments between April 23, 1991 and April 25, 1991 that have the Jupiter disk within the field of view. The times for each segment are listed below in Table 4. Due to the low count rates in each of the individual data segments the portion of the image which contained the disk of Jupiter (with a factor of two spatial margin) was extracted from each of the nine data segments, individual background subtractions using clear sky were performed, and the resulting data was combined into a single spectra. Therefore no information exist about the possible variation of the spectra as a function of Jupiter rotational phase. However, the single spectrum has been thoroughly analyzed in the context of a best fit bremsstrahlung and a best fit two emission line model. The data along with the results of these best fit models are shown in Figure 4. Please note that the model fits have been convolved with the proper energy resolution and energy dependent quantum efficiencies to allow a comparison with the extracted PSPC data. Therefore, the data shown are not to be interpreted as spectra, but as spectra convolved with the PSPC response function. Although, the signal to noise is low in the data set due to the small amount of on-Jupiter observation time in the present data set, the two line model is clearly a better fit with a chi square that is over a factor of two better than the best fit bremsstrahlung model (and also a factor of two better than the best power law fit which is not shown in the figure).

## ROSAT Discussion

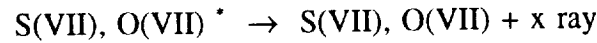
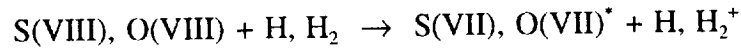
The total x ray power inferred from the analysis is  $1.3$  to  $2.1 \times 10^9$  Watts depending on whether the model fit assumed is the two line or the bremsstrahlung, respectively. This is within a factor of three of the  $4 \times 10^9$  Watts reported from the Metzger et al. [1983] Einstein x ray observations. The observed comparison is within variations that are associated with changes in the ultraviolet auroral output [Livengood, 1991]. Furthermore, in agreement with Metzger et al. we conclude that from bremsstrahlung x ray modeling that the model efficiency ( $5.6 \times 10^{-7}$ ; Waite, 1991) suggests that over  $3 \times 10^{15}$  Watts of auroral electron precipitation would be required to produce the observed x ray emission from an electron bremsstrahlung source. However, the factor of two better energy resolution available with ROSAT (as compared to Einstein) also allows a spectral interpretation of the results. This data as shown in Figure 4 suggests that a two line emission model produces a better fit (by a factor of two in chi square) than does the best bremsstrahlung fit. Yet the line model fit has two components, a narrow component near 0.2 KeV and a broader component centered at 0.9 KeV, which are not consistent with the Metzger et al. interpretation of S and O K-shell emission at 2.3 and 0.52 KeV, respectively. Reference to the soft x ray emission tables of Raymond and Smith [1977] does indicate a series of S(VII) recombination lines near 0.2 KeV and a series of O(VII) recombination lines near 0.9 KeV which are strong candidates for explaining the observed emissions (see Figure 5). The production of these emission lines occurs as a result of recombination lines that are produced from the slowing of the energetic ion beam as it enters the Jupiter upper atmosphere.

Charge state equilibrium of the ion beam in the atmosphere results from competition between electron capture and stripping which are charge state and energy dependent.



We estimate that in the electron capture process 10% of the reaction exothermicity goes into the excitation of recombination lines. If the initial charge states are S(VII) and O(VII) the resulting emission is in the soft x ray wavelength regime.

Recombination excitation:



The high charge states necessary to produce these emissions are the result of the incident ion beam energy and the fact that electron stripping and capture processes result in a rapid charge state equilibrium being established as the beam encounters the upper atmosphere. This point is illustrated (Figure 6) for energetic oxygen where we have presented the equilibrium fraction of the various charge states as a function of beam energy (results from private communication with T. E. Cravens, 1992). The figure indicates that an O(VII) charge state will occur for all ions that enter the atmosphere with an energy greater than ~700 KeV per amu. That such ions exist in the Jupiter magnetosphere and probably precipitate between L=7 and 10 has been demonstrated using Voyager data by Gehrels and Stone [1983]. They estimate that between  $10^{12}$  and  $10^{13}$  Watts of oxygen and sulfur with energies greater than 700 KeV per amu is precipitating into the Jupiter. This implies that an efficiency of 0.01 to 0.1% is required from x ray recombination processes to explain the present x ray aurora in a manner consistent with the observed loss of energetic oxygen and sulfur by Voyager [Gehrels and Stone, 1983]. Such an efficiency appears to be quite reasonable in the context of the modeling of energetic oxygen aurora at Jupiter by Horanyi et al. [1988] and detailed modeling calculations are now in progress.

However, we further note that as pointed out by Gehrels and Stone [1983] the observed energetic ion precipitation does not contain sufficient power to explain the observed ultraviolet aurora and extrapolations to 40 KeV per amu are required to supply this additional power. Such an extrapolation is not necessary to explain the observed x ray emissions. We therefore, conclude that in light of the HST Ulysses results, both electrons and ions play a role in the Jupiter auroral emissions, but that the bulk of the ultraviolet emissions (and thus a major portion of the power input) comes from electron processes, which result from processes in the outer magnetosphere and not from energetic ions precipitating from the middle magnetosphere. Such a scenario forms the new paradigm of the Earth-like aurora at Jupiter.



## References

- Acuña, M. H., and N. F. Ness, Results from the GSFC fluxgate magnetometer on Pioneer 11, in *Jupiter*, edited by T. Gehrels, p. 830-847, University of Arizona Press, Tucson, 1976.
- Broadfoot, A. L., et al., Overview of the Voyager ultraviolet spectrometry results through Jupiter encounter, *J. Geophys. Res.*, **86**, 8259-8284, 1981.
- Caldwell, J., A. T. Tokunga, and G. S. Orton, Further observations of 8  $\mu$ m polar brightenings of Jupiter, *Icarus*, **53**, 133-140, 1983.
- Caldwell, J., A. T. Tokunga, and F. C. Gillett, Possible infrared aurorae on Jupiter, *Icarus*, **44**, 667-675, 1980.
- Caldwell, J., *EOS*???
- Clarke, J. T., H. W. Moos, S. K. Atreya, and A. L. Lane, Observations from Earth orbit and variability of the polar aurora on Jupiter, *Astrophys. J. (Lett.)*, **241**, L179-182, 1980.
- Dols, V., J. C. Gerard, F. Paresce, R. Prange, and A. Vidal-Madjar, Ultraviolet imaging of the Jovian aurora with the Hubble Space Telescope, in press *GRL*, 1992.
- Gehrels, N., and E. C. Stone, Energetic oxygen and sulfur ions in the Jovian magnetosphere and their contribution to the auroral excitation, *J. Geophys. Res.*, **88**, 5537-5550, 1983.
- Gladstone, G. R., and T. E. Skinner, Spectral analysis of Jovian auroral emissions, in *Time-Variable Phenomena in the Jovian System*, M. J. S. Belton, R. A. West, and J. Rahe, Eds., NASA SP-494, Washington, D. C., 221-228, 1989.
- Herbert, F., B. R. Sandel, and A. L. Broadfoot, Observations of the Jovian UV aurora by Voyager, *J. Geophys. Res.*, **92**, 3141-3154, 1987.
- Horanyi, M., T. E. Cravens, and J. H. Waite, Jr., The precipitation of energetic heavy ions into the upper atmosphere of Jupiter, *J. Geophys. Res.*, **93**, 7251-7271, 1988.
- Lanzerotti, L. J., T. P. Armstrong, R. E. Gold, K. A. Anderson, S. M. Krimigis, R. P. Lin, M. Pick, E. C. Roelof, E. T. Sarris, G. M. Simnett, C. G. MacLennan, H. T. Choo, and S. J. Tappin, Hot plasma environment at Jupiter: Ulysses results, in press *Science*, 1992.
- Livengood, T. A., R. M. Prangé, G. E. Ballester, and H. W. Moos, Exceptional variability of the Jovian ultraviolet aurora of December 1990: Primary particle energy and identity?, *EOS Trans. AGU*, **72**, 185, 1991.
- Metzger, A. E., D. A. Gilman, J. L. Luthy, K. C. Hurley, H. W. Schnopper, F. D. Seward, and J. D. Sullivan, The detection of X-Rays from Jupiter, *J. Geophys. Res.*, **88**, 7731-7741, 1983.
- Raymond, J. C., and B. W. Smith, Soft x ray spectra of a hot plasma, *App. J. Suppl.*, **35**, 419-439, 1977.
- Sandel, B. R., et al., Extreme ultraviolet observation from Voyager 2 encounter with Jupiter, *Science*, **206**, 962-966, 1979.
- Waite, J. H., Jr., Comment on "Bremsstrahlung X rays from Jovian auroral electrons" by D. D. Barbosa, *J. Geophys. Res.*, **96**, 19,529-19,532, 1991.
- Waite, J. H., Jr., J. T. Clarke, T. E. Cravens, and C. M. Hammond, The Jovian aurora: Electron or ion precipitation?, *J. Geophys. Res.*, **93**, 7244-7250, 1988.
- Waite, J. H., Jr., et al., Electron precipitation and related aeronomy of the Jovian thermosphere and ionosphere, *J. Geophys. Res.*, **88**, 6143-6163, 1983.
- Yung, Y. L., et al.,  $H_2$  fluorescence spectrum from 1200 to 1700Å by electron impact: Laboratory study and application to Jovian aurora, *Astrophys. J. (Lett.)*, **254**, L65, 1982.

Yung, Y. L., and D. F. Strobel, Hydrocarbon photochemistry and Lyman alpha albedo of Jupiter, *Astrophys. J.*, 238, 395-402, 1980.

## Figure Captions

Figure 1a. Model Jovian auroral spectrum of the H Lyman alpha and H<sub>2</sub> band emissions.

Figure 1b. The convolution of the model spectrum with the wavelength dependent filter and quantum efficiencies response curves for the HST FOC F130M/F140W.

Figure 3. Ten by ten block averaged representation of the full set of HST FOC images with boxes indicating positions of intensity information extraction.

Figure 4. Combined ROSAT PSPC photon energy spectrum and the model curves for a best fit two line model and a best fit bremsstrahlung model convoluted with the detector response function.

Figure 5. Two line model fit and the wavelength location and relative intensity of known recombination emission lines from S(VII) and O(VII).

Figure 6. Equilibrium fraction for O<sup>+q</sup> (q = 0, 8) charge state distributions as a function of ion energy.

Table 1. HST Jovian Auroral Observations

| <u>I#</u> | <u>DATE</u> | <u>TIME(UT)</u> | <u>CML(S<sub>in</sub>L)</u> | <u>POLE</u> | <u>Intensity(kR)</u> | <u>Area("²)</u> | <u>Power(W)*</u>                        |
|-----------|-------------|-----------------|-----------------------------|-------------|----------------------|-----------------|-----------------------------------------|
| 101a      | 2/6/92      | 2:40            | 168                         | North       | 34 +/- 23            | 2.9             | 5x10 <sup>10</sup> - 7x10 <sup>11</sup> |
| 101b      | 2/6/92      | 2:40            | 168                         | North       | 13 +/- 14            | 2.8             | 0 - 5x10 <sup>12</sup>                  |
| 101c      | 2/6/92      | 2:40            | 168                         | North       | 31 +/- 34            | 1.1             | 0 - 2x10 <sup>13</sup>                  |
| 102       | 2/6/92      | 4:08            | 222                         | North       | High Noise           | ---             | ---                                     |
| 201a      | 2/7/92      | 9:07            | 43                          | South       | 12 +/- 11            | 4.8             | 1x10 <sup>10</sup> - 5x10 <sup>11</sup> |
| 201b      | 2/7/92      | 9:07            | 43                          | South       | 24 +/- 18            | 2.5             | 2x10 <sup>10</sup> - 5x10 <sup>11</sup> |
| 202       | 2/7/92      | 10:34           | 95                          | South       | 49 +/- 30            | 1.7             | 1x10 <sup>11</sup> - 5x10 <sup>11</sup> |
| 301       | 2/8/92      | 23:46           | 5                           | South       | Low Signal           | ---             | ---                                     |
| 302a      | 2/9/92      | 1:11            | 56                          | South       | 26 +/- 21            | 2.6             | 1x10 <sup>10</sup> - 5x10 <sup>11</sup> |
| 302b      | 2/9/92      | 1:11            | 56                          | South       | 8 +/- 16             | 2.1             | 0 - 4x10 <sup>12</sup>                  |
| 401       | 2/9/92      | 9:24            | 355                         | South       | Low Signal           | ---             | ---                                     |
| 402a      | 2/9/92      | 10:50           | 47                          | South       | 41 +/- 28            | 1.8             | 2x10 <sup>10</sup> - 1x10 <sup>12</sup> |
| 402b      | 2/9/92      | 10:50           | 47                          | South       | 22 +/- 24            | 1.6             | 0 - 1x10 <sup>13</sup>                  |

\* Range limits include not only 1 sigma measurement uncertainties, but also a factor of 2 uncertainty due to unaccounted for atmospheric absorption, a factor of 2-4 increase from the optical defects of HST which depends on the size of the emission region, and an upper limit to the size of the emitting area

Table 2. Spectra for Caldwell, Stern, and Paresce

| <u>BAND</u>          | <u>CALDWELL</u><br><u>(F140W, F152M)</u> | <u>STERN</u><br><u>(F130M, F140W)</u> | <u>PARESCCE</u><br><u>(F120M, F140W)</u> |
|----------------------|------------------------------------------|---------------------------------------|------------------------------------------|
| Lya                  | 0.034                                    | 0.340                                 | 0.828                                    |
| 1230-1650            | 0.962                                    | 0.648                                 | 0.149                                    |
| 1230-1300            | 0.015                                    | 0.385                                 | 0.106                                    |
| 1557-1619            | 0.290                                    | 0.010                                 | 0.004                                    |
| Total<br>(cps/pixel) | 1.64E-5                                  | 6.21E-6                               | 1.29E-5                                  |

Table 3. HST FOC Intensity Determination

| <u>DESIGNATED IMAGE BLOCK</u> |                                               | <u>IMAGE COORDINATES</u><br><u>[X1:X2, Y1:Y2]</u> | <u>AVERAGE COUNTS</u><br><u>AND VARIANCE</u><br><u>(per pixel)</u> |
|-------------------------------|-----------------------------------------------|---------------------------------------------------|--------------------------------------------------------------------|
| Image 101                     | 101a                                          | [16:23, 14:23]                                    | 0.95±0.21                                                          |
|                               | 101b                                          | [10:16, 28:38]                                    | 0.74±0.11                                                          |
|                               | 101c                                          | [31:35, 4:10]                                     | 0.73±0.10                                                          |
|                               | bc1(101)                                      | [5:13, 3:13]                                      | 0.63±0.09                                                          |
|                               | [off planet]                                  |                                                   |                                                                    |
|                               | bc2(101)                                      | [34:44, 34:44]                                    | 0.61±0.09                                                          |
|                               | [on planet, no aurora]                        |                                                   |                                                                    |
| Image 102                     | no analysis attempted due to high noise level |                                                   |                                                                    |
| Image 201                     | 201a                                          | [10:18, 25:38]                                    | 0.90±0.16                                                          |
|                               | 201b                                          | [36:42, 2:11]                                     | 0.91±0.12                                                          |
|                               | bc1(201)                                      | [4:14, 4:14]                                      | 0.62±0.08                                                          |
|                               | bc2(201)                                      | [25:35, 25:35]                                    | 0.70±0.10                                                          |
| Image 202                     | 202                                           | [20:26, 22:28]                                    | 0.88±0.14                                                          |
|                               | bc1(202)                                      | [5:15, 5:15]                                      | 0.56±0.09                                                          |
|                               | bc2(202)                                      | [30:40, 30:40]                                    | 0.60±0.09                                                          |
| Image 301                     | no analysis attempted due to low signal level |                                                   |                                                                    |
| Image 302                     | 302a                                          | [29:37, 7:14]                                     | 1.00±0.16                                                          |
|                               | 302b                                          | [24:29, 20:29]                                    | 0.83±0.12                                                          |
|                               | bc1(302)                                      | [5:15, 5:15]                                      | 0.66±0.09                                                          |
|                               | bc2(302)                                      | [30:40, 30:40]                                    | 0.77±0.11                                                          |
| Image 401                     | no analysis attempted due to low signal level |                                                   |                                                                    |
| Image 402                     | 402a                                          | [29:37, 4:9]                                      | 0.85±0.12                                                          |
|                               | 402b                                          | [24:29, 17:24]                                    | 0.71±0.10                                                          |
|                               | bc1(402)                                      | [5:15, 5:15]                                      | 0.52±0.09                                                          |
|                               | bc2(402)                                      | [30:40, 30:40]                                    | 0.59±0.08                                                          |

Table 4. Segment Times

| START<br><u>(UT)</u> |          | <u>STOP</u> |
|----------------------|----------|-------------|
| 4/23/91              | 12:52:32 | 13:01:55    |
| 4/23/91              | 22:03:42 | 22:31:58    |
| 4/24/91              | 03:11:37 | 03:26:58    |
| 4/24/91              | 12:51:27 | 13:00:54    |
| 4/24/91              | 19:00:44 | 19:12:41    |
| 5/24/91              | 03:10:28 | 03:24:53    |
| 5/24/91              | 11:15:52 | 11:23:17    |
| 5/24/91              | 12:42:06 | 12:59:11    |
| 5/24/91              | 17:22:04 | 17:40:20    |

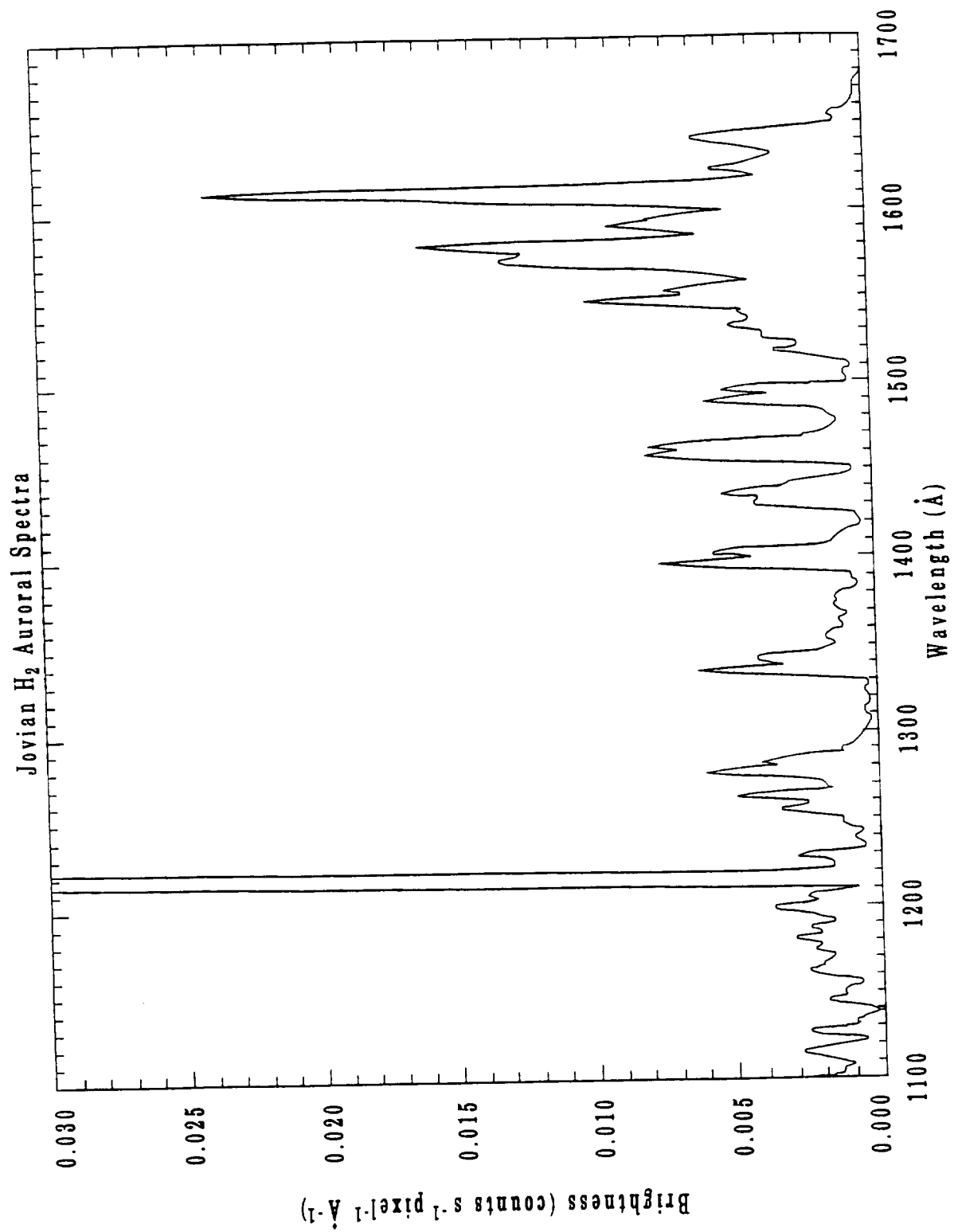


Figure 1a

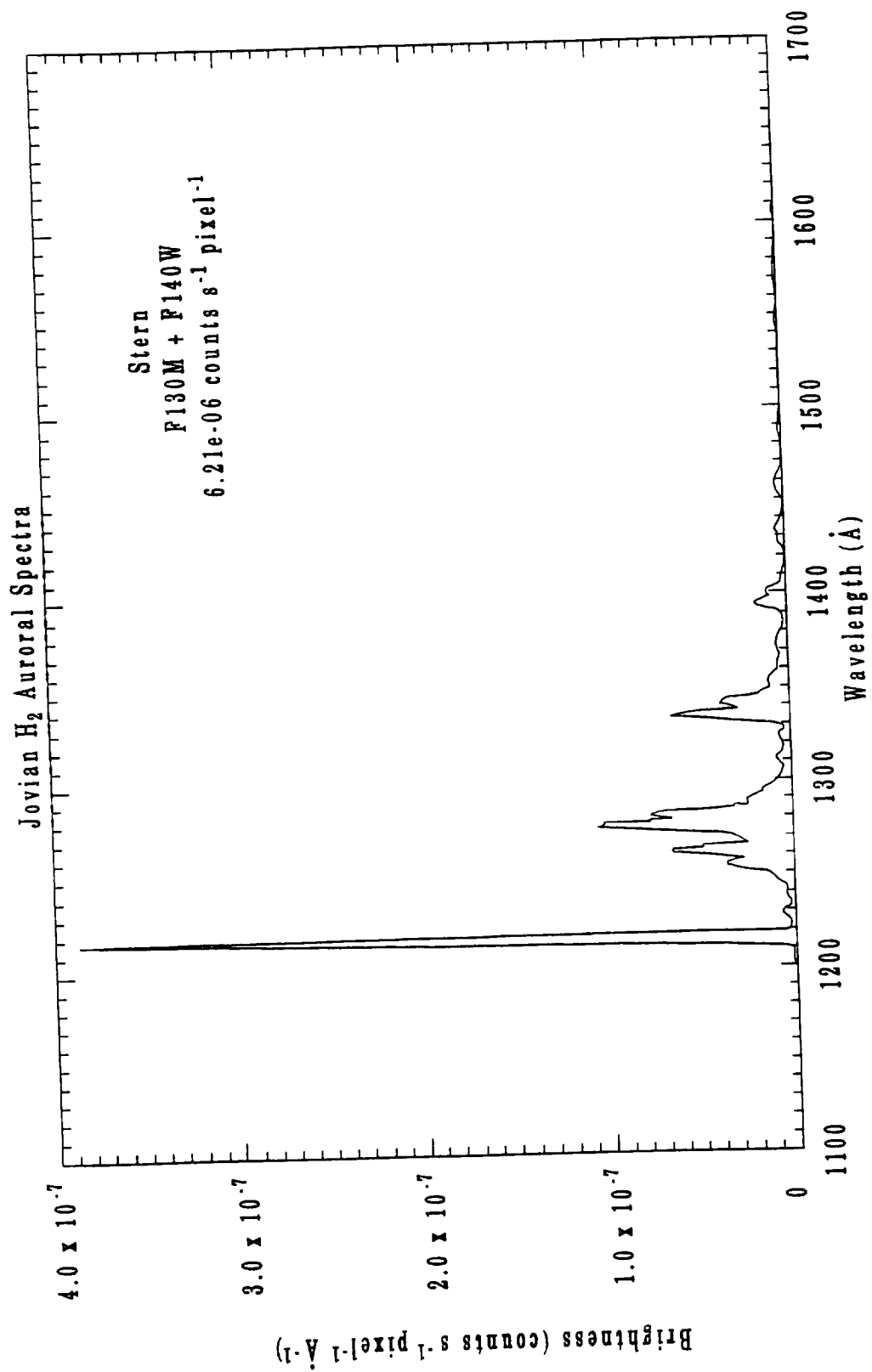
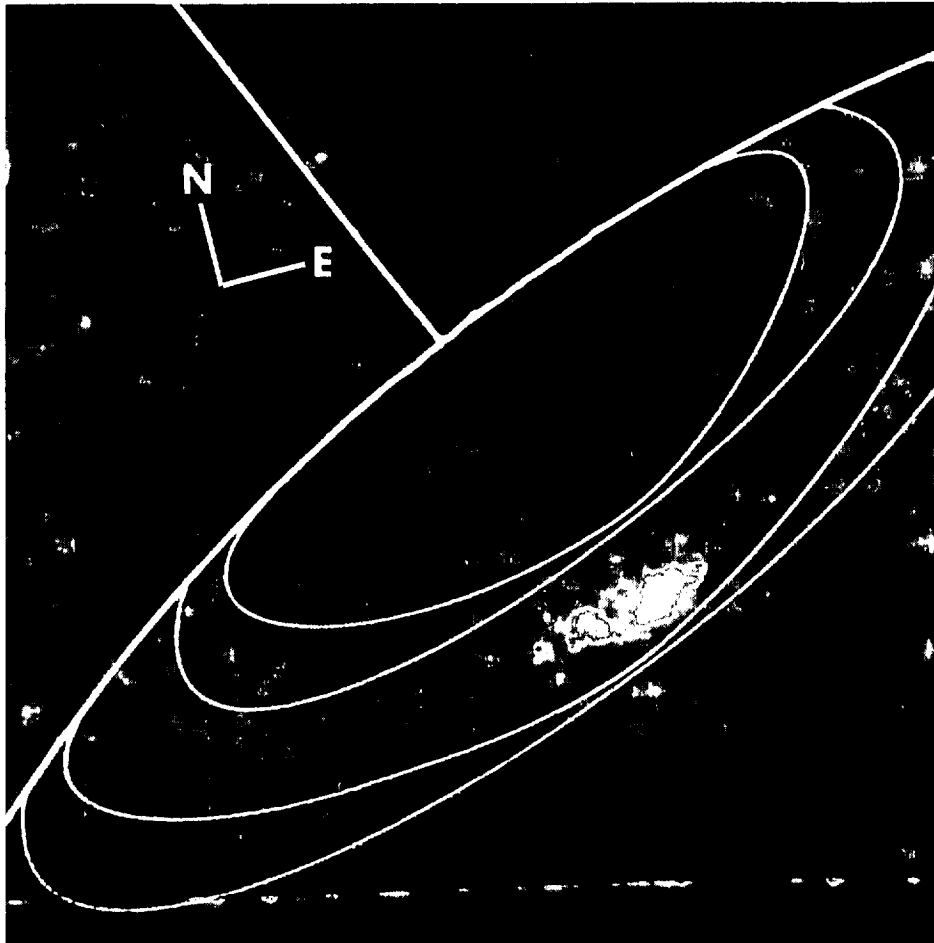


Figure 1b



ORIGINAL PAGE  
COLOR PHOTOGRAPH



**Figure 2a.** Reduced HST FOC image of the north pole showing bright auroral features and shading that indicate Jovian magnetic coordinates for Io plasma torus auroral zone low latitude circle and magnetopause auroral zone smaller inner circle.

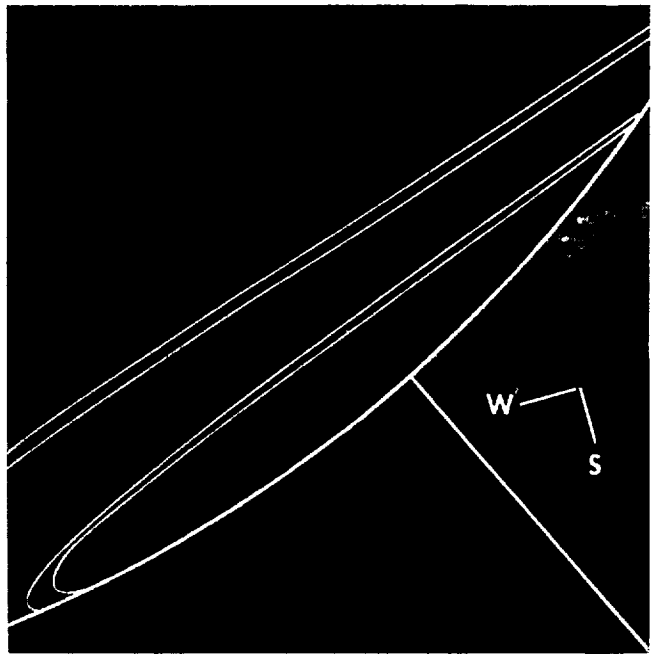
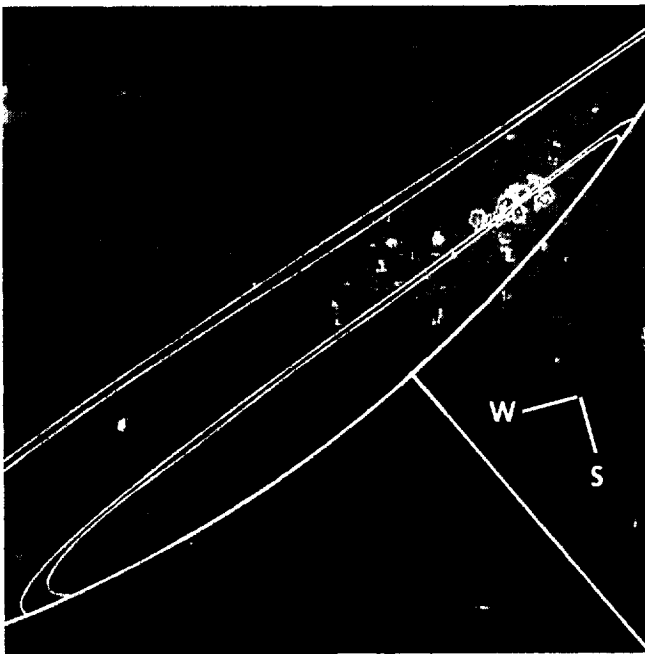
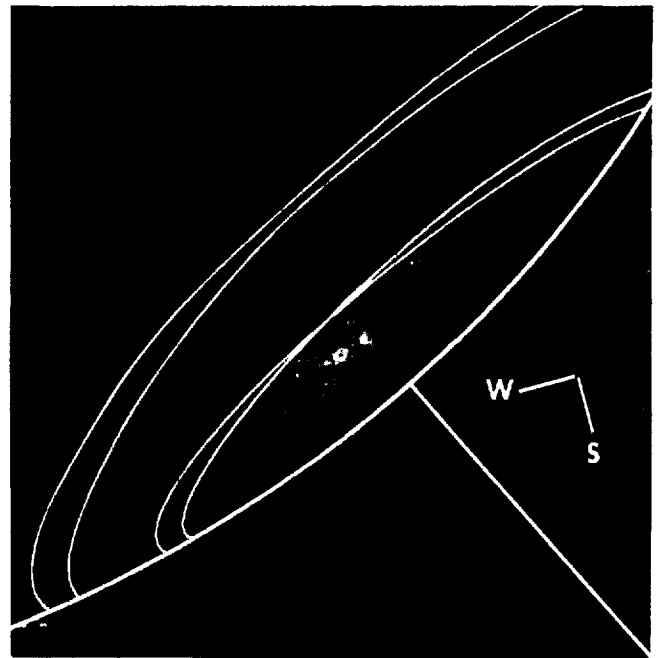
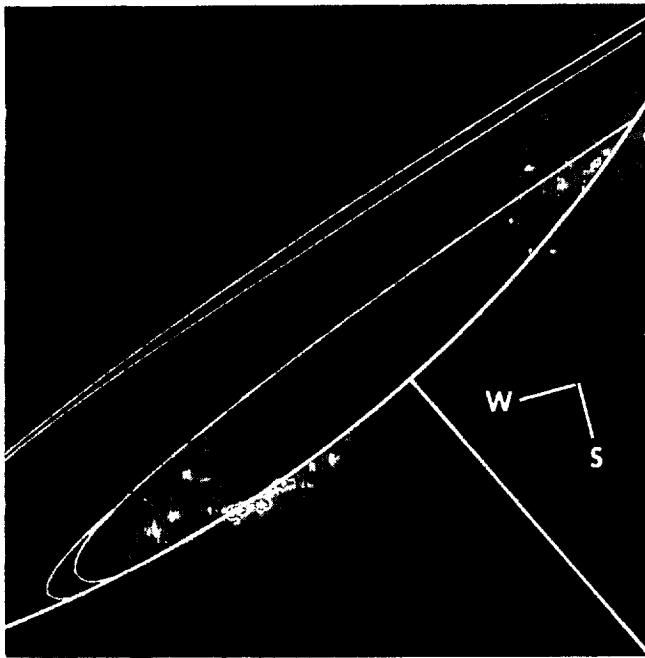


**Figure 2b.** Reduced HST FOC images of the south pole showing bright auroral features and shading that indicate Jovian magnetic coordinates for Io plasma torus auroral zone low latitude circle and magnetopause auroral zone smaller inner circle.

CPD 10-100  
GOLD PHOTOGRAPH

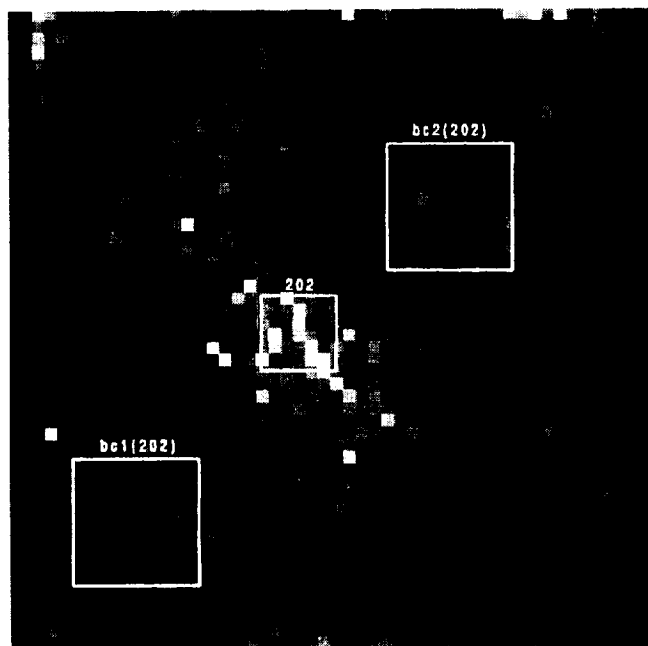
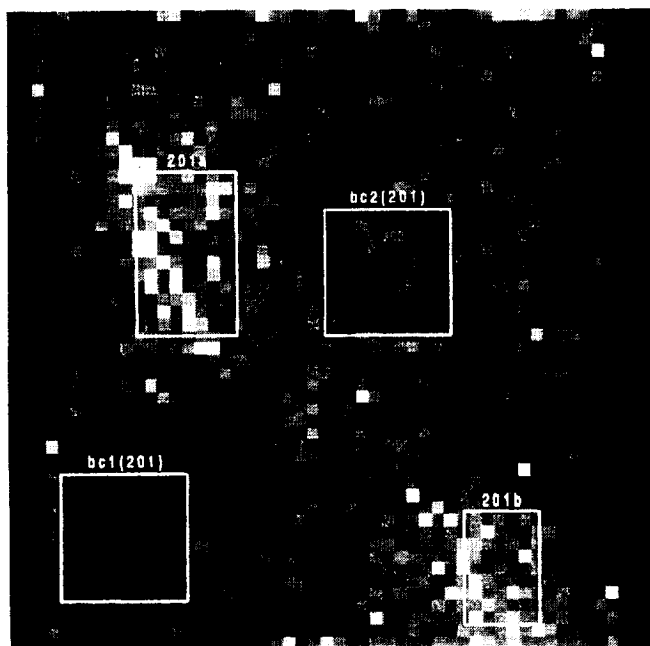
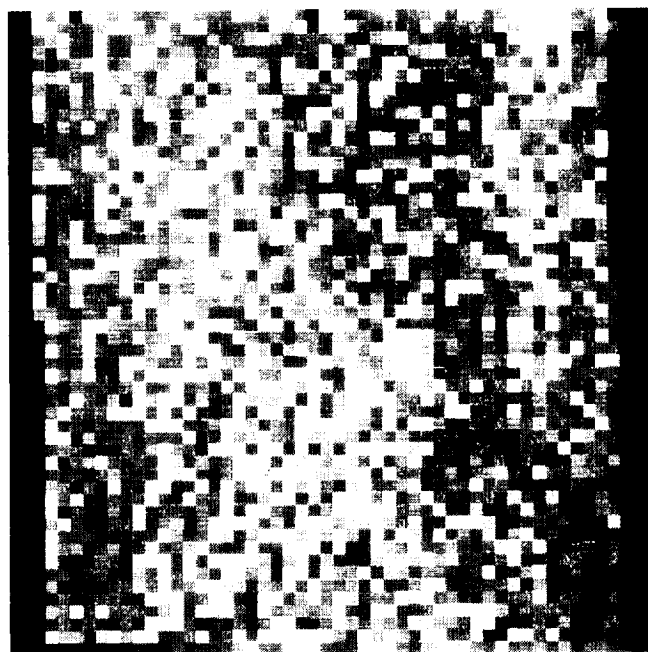
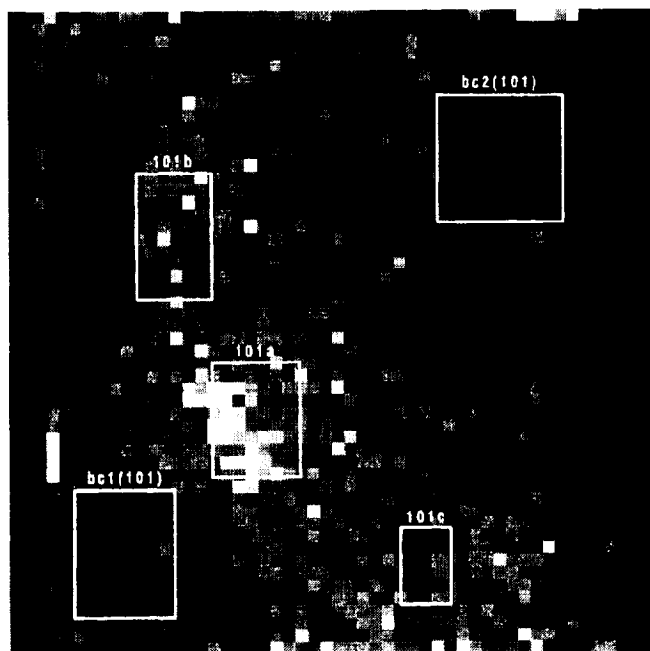


Figure 3a

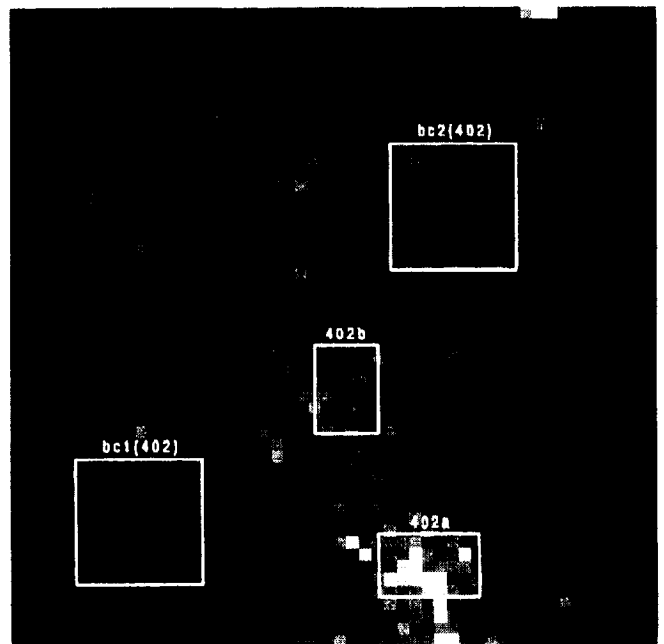
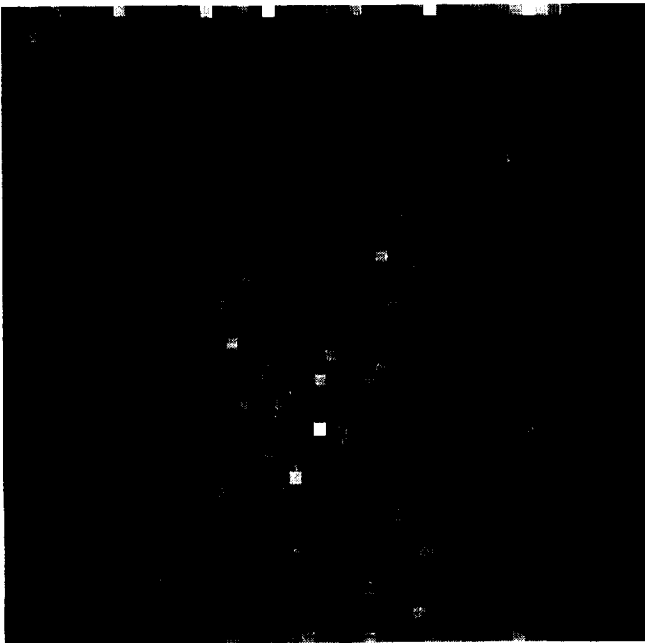
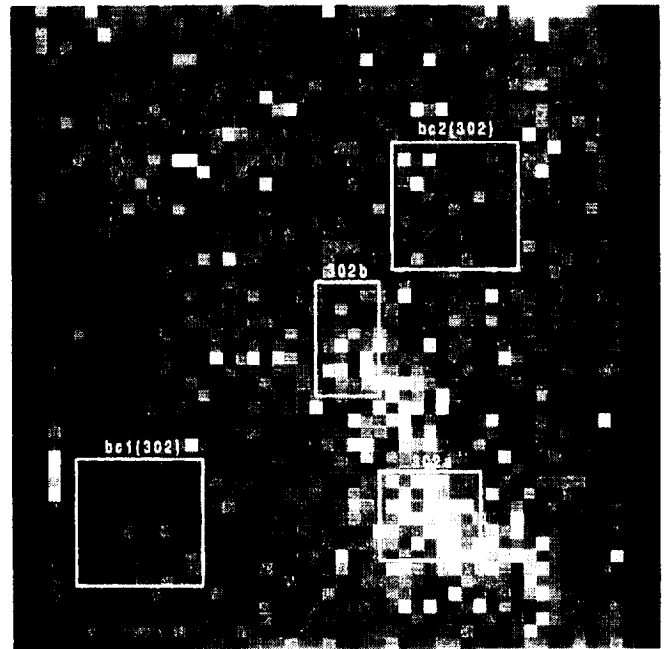
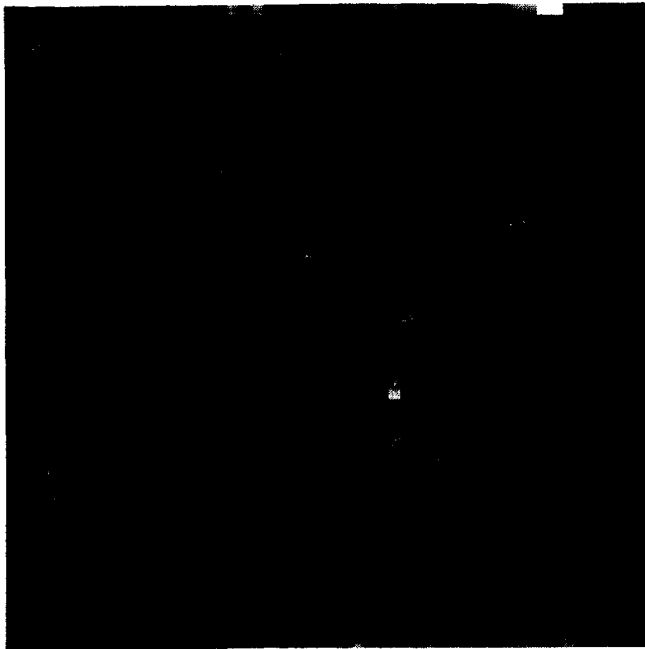


Figure 3b

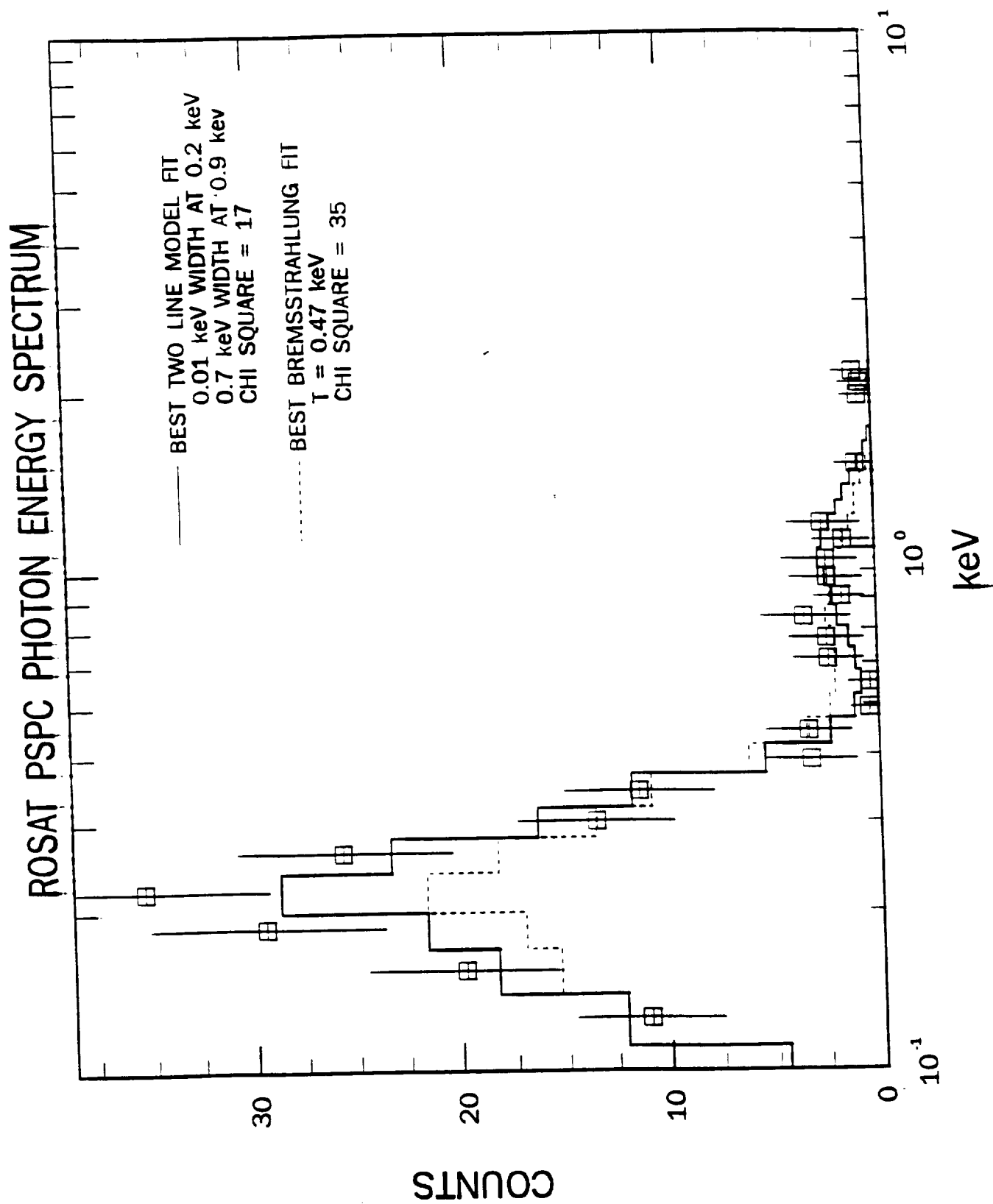


Figure 4

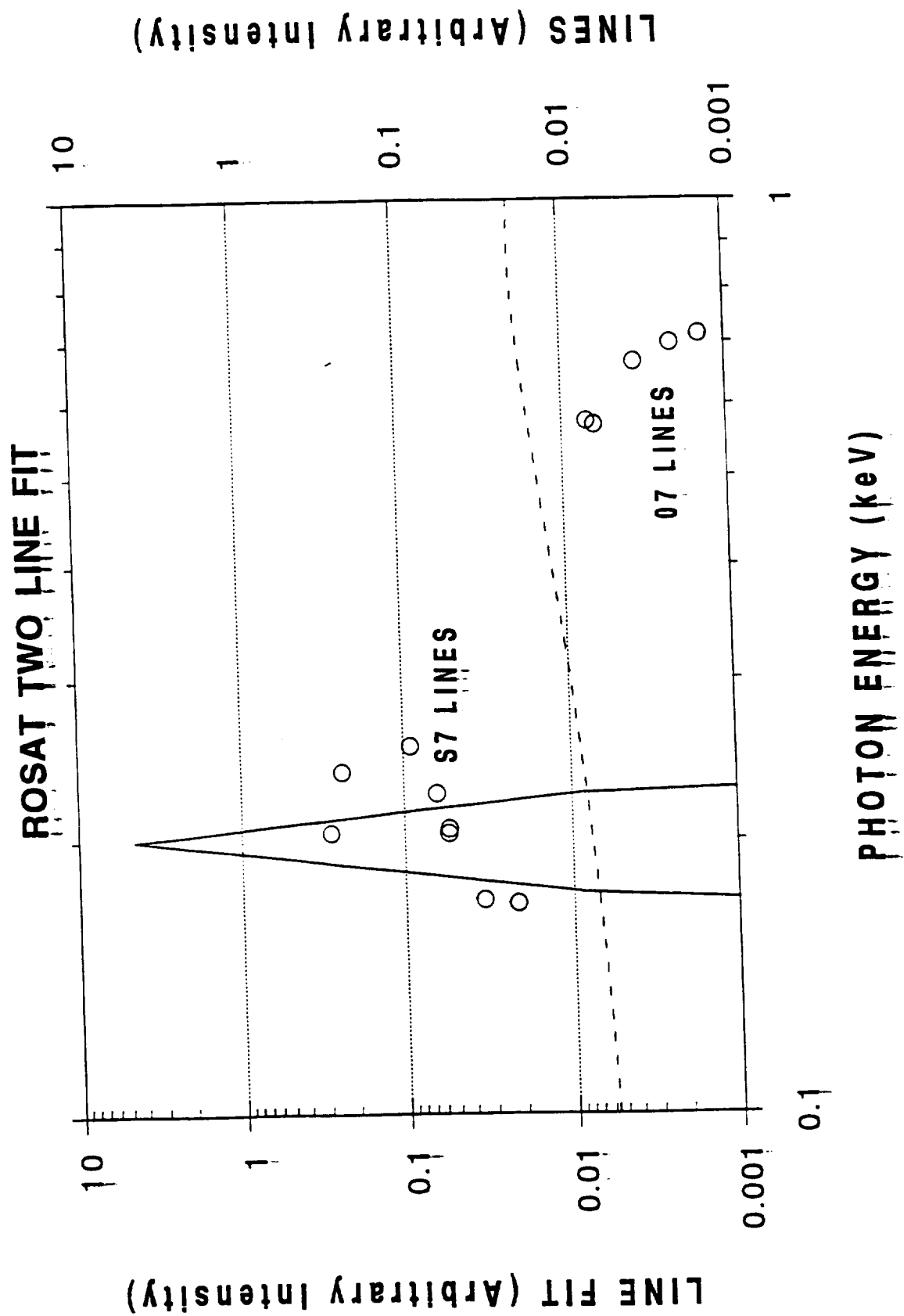


Figure 5

# OXYGEN CHARGE STATE FRACTIONS

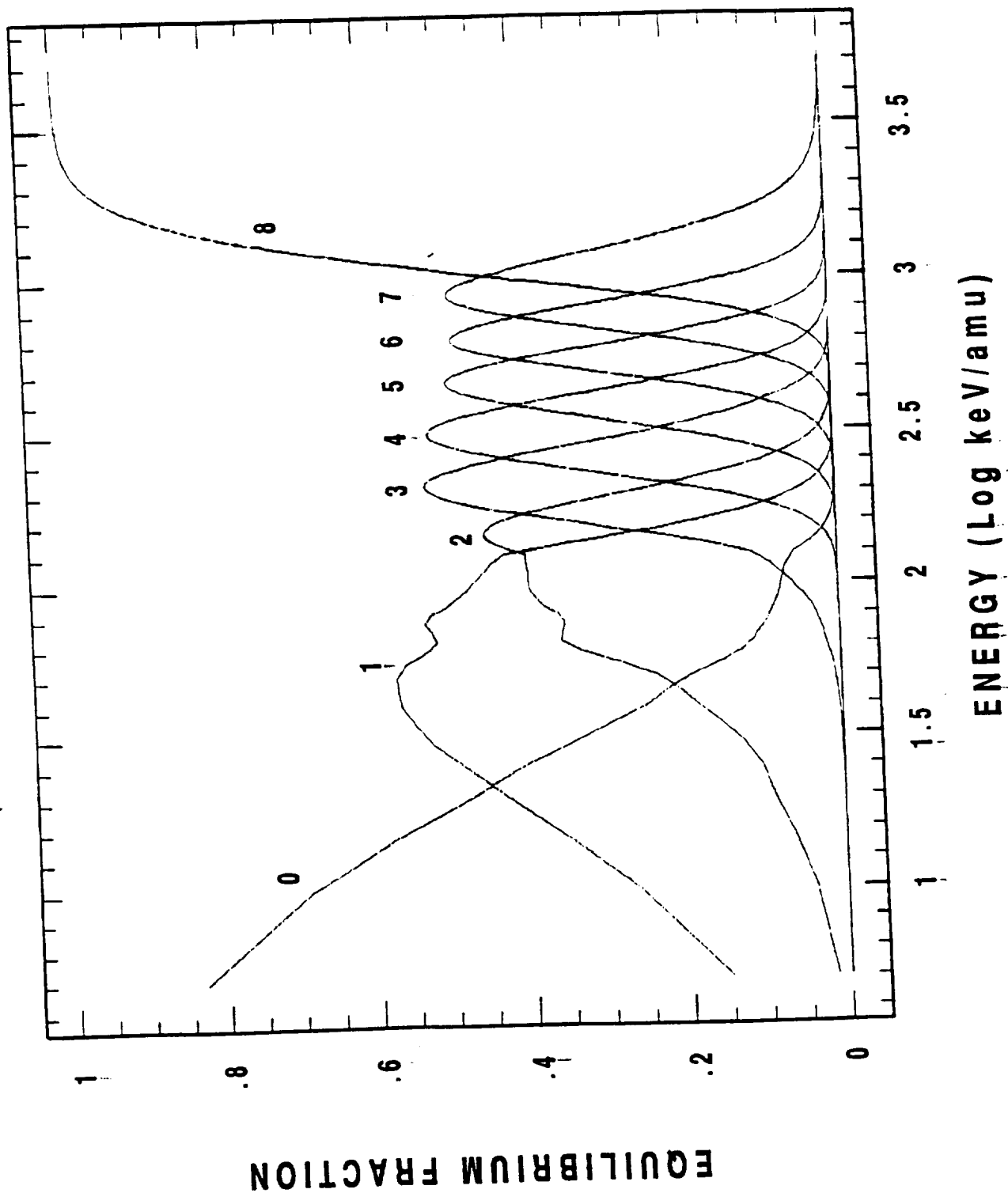


Figure 6

